UNIVERSITY *of*York

This is a repository copy of *The spatial distribution of HO2in an atmospheric pressure plasma jet investigated by cavity ring-down spectroscopy*.

White Rose Research Online URL for this paper:
https://eprints.whiterose.ac.uk/id/eprint/166206/

Version: Published Version

Article:

White Rose
university consortium
Universities of Leeds, Sheffield & York

eprints@whiterose.ac.uk
https://eprints.whiterose.ac.uk/

The spatial distribution of HO_2 in an atmospheric pressure plasma jet investigated by cavity ring-down spectroscopy

View the article online for updates and enhancements.

The spatial distribution of HO$_2$ in an atmospheric pressure plasma jet investigated by cavity ring-down spectroscopy

S-J Klose[1,4] , **K M Manfred**[2] , **H C Norman**[3], **G A D Ritchie**[3] and
J H van Helden[1]

[1] Leibniz Institute for Plasma Science and Technology (INP), Felix-Hausdorff-Str. 2, 17489 Greifswald, Germany
[2] Department of Chemistry, University of York, Heslington, York, YO10 5DD, United Kingdom
[3] Department of Chemistry, Physical and Theoretical Chemistry Laboratory, University of Oxford, South Parks Road, Oxford, OX1 3QZ, United Kingdom

E-mail: sarah-johanna.klose@inp-greifswald.de

CrossMark

Abstract

Cold atmospheric pressure plasma jets make important contributions to a range of fields, such as materials processing and plasma medicine. In order to optimise the effect of those plasma sources, a detailed understanding of the chemical reaction networks is pivotal. However, the small diameter of plasma jets makes diagnostics challenging. A promising approach to obtain absolute number densities is the utilisation of cavity-enhanced absorption spectroscopy methods, by which line-of-sight averaged densities are determined. Here, we present first measurements on how the spatial distribution of HO$_2$ in the effluent of a cold atmospheric pressure plasma jet can be obtained by cavity ring-down spectroscopy in an efficient way. Instead of recording fully wavelength resolved spectra, we will demonstrate that it is sufficient to measure the absorption coefficient at two wavelengths, corresponding to the laser being on and off the molecular resonance. By sampling the effluent from the 1.6 mm diameter nozzle in the radial direction at various axial positions, we determined that the distances over which the HO$_2$ density was distributed were (3.9 ± 0.5) mm and (6.7 ± 0.1) mm at a distance of 2 mm and 10 mm below the nozzle of the plasma jet, respectively. We performed an Abel inversion in order to obtain the spatial distribution of HO$_2$ that is presented along the symmetry axis of the effluent. Based on that localised density, which was $(4.8 \pm 0.6) \cdot 10^{14}$ cm^{-3} at the maximum, we will discuss the importance of the plasma zone for the production of HO$_2$.

Keywords: spatial distribution, cavity ring-down spectroscopy, atmospheric pressure plasma jet, density of transient species, hydroperoxyl radical

(Some figures may appear in colour only in the online journal)

1. Introduction

With the development of cold atmospheric pressure plasma jets (CAPJs) over the last decade, the localised and selective treatment of heat sensitive objects and biological tissue has gained high industrial and medical importance thereby widening established fields, such as materials processing, and opening new fields, such as plasma medicine and plasma agriculture [1–5]. The number of applications for CAPJs increases continuously and their adaptability becomes more and more important, in particular for their utilisation for decontamination, sterilisation, wound healing and cancer therapy [6–10]. It is therefore essential to diagnose the fluxes of the plasma generated species and to identify the relevant reaction pathways which occur under different conditions, such as feed gas and surrounding gas compositions, in order to obtain a detailed understanding of the chemical reaction network and thus to be able to tailor the reactive species composition for a specific application.

Previous studies have shown that the individual composition of reactive species can be changed by adding molecular gases to the argon feed gas or by changing the surrounding gas composition [11, 12]. For example, it was demonstrated that the addition of water to the feed gas of a CAPJ reduces the ozone production [13], and by the addition of a few thousand ppm oxygen to the feed gas, the NO production could be controlled [14]. By changing the surrounding gas composition, a mixture of oxygen and nitrogen, the ozone density increased, whereas the number of reactive oxygen–nitrogen species (RONS) decreased with rising oxygen concentration in the surrounding atmosphere. These are important observations, as RONS seem to play an important role in the plasma-driven effects on biological tissue [15–17].

One of the key species identified in plasma-treated liquids and in cell culture media is hydrogen peroxide, H_2O_2, which is known to induce oxidative stress on cells that reduces the cell viability and leads to the programmed cell death at high concentrations [13, 15]. A contemporary question for understanding the plasma-to-liquid interaction is to determine the location where cell-effective species, such as H_2O_2, are produced: Are they formed in the gas phase and diffuse into the liquid or are they formed inside the liquid via secondary reactions?

There are two dominant species, which are involved in the production and destruction of H_2O_2: The hydroxyl radical, OH, and the hydroperoxyl radical, HO_2 [18]. Both radicals are known precursors that drive the low temperature oxidation chemistry. The HO_2 radical, in particular, is involved in biological oxidation reactions, such as lipid peroxidation [19], as it can enter cell membranes. In a liquid, a chemical equilibrium will develop between HO_2 and the superoxide anion, O_2^-, which is responsible for a change of the pH-value in plasma-treated liquids [20].

The dissociation of water, ubiquitous in the atmosphere, plays an important role on the formation of both OH and HO_2; OH is a direct product of water splitting, while HO_2 is formed by the reaction of the hydrogen atom co-product, H, with oxygen molecules, O_2. In order to gain better insights into the role

of HO_2, it is crucial to determine its gas phase density and to follow its reaction pathways in the effluent.

However, the small diameter of CAPJs (in the range of mm) makes diagnostics challenging. A common technique to detect the most abundant fluxes of molecules and selected electronically excited atoms, such as metastable Ar or He, is absorption spectroscopy, as it provides absolute number densities if the absorption cross-sections are known [21, 22]. Additionally, the utilization of high-finesse optical cavities enhances the effective absorption path length and thus the sensitivity, which is crucial for the detection of highly reactive transient species in CAPJs. Within such a cavity, which normally consists of two highly reflective mirrors, the effective absorption path length through the sample under investigation can easily be increased by a factor of thousand to ten thousand [23, 24]. With cavity-enhanced spectroscopy techniques, detection limits of parts-per-million (ppm) up to parts-per-trillion (ppt) can be achieved, as for example shown for methane in reference [25]. For the detection of species in plasmas, cavity ring-down spectroscopy has been the most widely used cavity-enhanced spectroscopy technique. Some applications of CRDS for the analysis of atmospheric pressure plasma jets, including the detection of N_2^+, $N_2(A)$, OH and He^*, are reported in references [22, 26, 27]. In order to detect HO_2 radicals in the effluent of a CAPJ, Gianella *et al* have recently applied optical feedback cavity-enhanced absorption spectroscopy (OF-CEAS) [28] and continuous wave cavity ring-down spectroscopy (cw-CRDS) [18]. The latter has the advantage to cover a broader wavelength range and to be less susceptible to fluctuations of the base line. Moreover, with CRDS, a higher sensitivity and shorter acquisition time could be achieved.

For the determination of the density from absorption spectra, Gianella *et al* developed a fitting routine that included 23 transitions of the second vibrational overtone of the OH stretch $(2\nu_1)$ in the HO_2 radical around 6638.2 cm^{-1} (1506 nm), as well as overlapping transitions from water that was present in the ambient atmosphere and in the feed gas [18].

Using a simple plug flow model, Gianella *et al* identified the most important production and consumption pathways for HO_2. HO_2 was mainly consumed by reactions with OH and H, whereas it was dominantly formed through the reaction of H and O_2.

In order to gain further insights into the formation and loss mechanism of HO_2, spatial information is required. However, obtaining spatial density distributions with absorption spectroscopy techniques is demanding, as commonly line-of-sight densities are determined, assuming a constant density that is homogeneously distributed over the effective absorption length l.

To obtain a first indication of the radial profile of the HO_2 density, Gianella *et al* sampled the effluent of a CAPJ through a pinhole expanding it to 5.33 kPa [18], while stepping the centre of the effluent relative to the centre of the pinhole. They measured a doughnut-like shape with the highest densities at the sides and a dip in the centre of the effluent representing a formation of HO_2 by the reaction of H atoms produced by water dissociation in the feed gas with O_2 molecules diffused

into the effluent from the surrounding atmosphere. The influence of the pinhole on the discharge was not investigated, but it was pointed out that it can not be excluded that the way, in which the low pressure experiment has been performed, is responsible for the observed profile.

In this work, we build upon those initial observations and show how spatially resolved density distributions in atmospheric pressure plasma jets can be obtained by cw-CRDS. By recording full spectra between 6637.6 cm^{-1} and 6638.7 cm^{-1} in the effluent of the kINPen plasma jet with an acquisition time of about 1 h each, as was done previously by Gianella *et al* [18], obtaining a spatial distribution becomes time consuming. We will show that by using an alternative technique, called the on/off-resonance method, the recording time can be reduced significantly. Instead of taking full spectra, we will demonstrate that measuring the absorption at two wavelengths is sufficient to determine the density of HO$_2$. By combining axial and radial scans and performing an Abel inversion, we determined a spatial map of the density of HO$_2$ in the effluent of the plasma jet.

The remainder of this work is organised as follows. In section 2, the plasma jet, the cw-CRDS spectrometer and the procedure to obtain densities from full spectra are described. Section 3 is divided into three parts: in the first part, section 3.1, the on/off-resonance method is explained and the determined absorption coefficients are compared to the absorption coefficients obtained from full spectra. In the second part, section 3.2, the effective absorption length at various axial positions in the effluent is determined. In the third part, section 3.3, it is explained how a spatial map of the HO$_2$ distribution can be obtained by performing an Abel inversion. Based on that spatial distribution of HO$_2$, the new insights into the reaction kinetics of HO$_2$ in the effluent of a CAPJ are discussed in section 4. The paper concludes with section 5, which provides a summary of the work.

2. Experimental setup

2.1. kINPen-Sci plasma jet

The plasma source investigated in this work, the so-called kINPen-Sci, is the scientific version of the kINPen, a CAPJ certified for medical applications. The device produces a guided streamer discharge, which is driven in a dielectric capillary (diameter: 1.6 mm) between a powered inner needle and a grounded outer ring at a frequency of about 1 MHz [29]. We operated the kINPen with 3 slm humidified Ar carrier gas (humidity: 3000 ppm). Therefore, 10% of the Ar flow was guided through a water bubbler held at room temperature [18, 28]. In order to control the effluent's surrounding gas environment, the kINPen was equipped with a gas curtain device maintaining a total oxygen flow rate of 5 slm [18].

2.2. Cavity ring-down spectrometer

The experimental setup of the cavity ring-down spectrometer is represented schematically in figure 1 and is the same setup previously used in reference [18].

A distributed feedback diode laser emitting at 1506.4 nm (6638.2 cm^{-1}) in a fibre-pigtailed butterfly
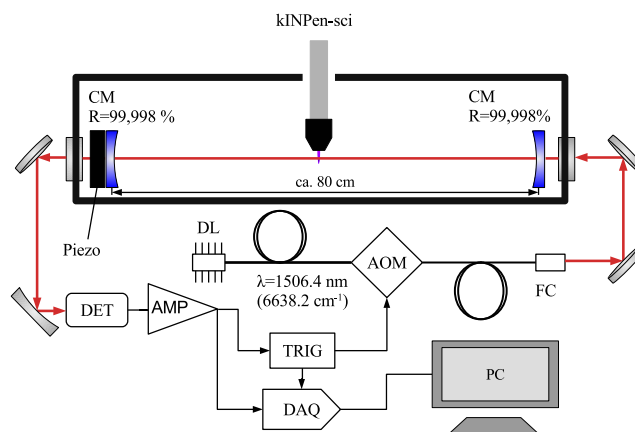
**Figure 1.** Schematic of the cw-CRDS setup for the HO$_2$ detection in the effluent of the CAPJ kINPen-sci. DL: diode laser, AOM: acousto-optic modulator, FC: fibre collimation package, CM: cavity mirror, Piezo: piezo-electric transducer, DET: detector, AMP: amplifier, TRIG: trigger circuit, DAQ: data acquisition module, PC: personal computer.

package (NLK1S5GAAA, NTT Electronics), whose current and temperature were controlled by a Thorlabs LDC200 current driver and a Thorlabs TED200 temperature controller, respectively, was directed via an adjustable fibre collimation package (CFC-8X-C, Thorlabs) and two protected silver coated mirrors into the optical cavity, consisting of two high reflectivity mirrors (Layertec, reflectivity $R = 99.998\%$, radius of curvature $r = 1$ m). These mirrors were separated by a distance of $L = 80$ cm, yielding a minimum beam diameter of 1 mm in the centre of the cavity. The output mirror was mounted on a hollow cylindrical piezoelectric transducer so that the length of the cavity could be modulated by a few laser wavelengths. The exiting light was then focused with an off-axis parabolic mirror onto an InGaAs photodiode (DET10C, Thorlabs), whose photocurrent was amplified by a transimpedance amplifier (DLPCA-200, FEMTO) and sent to a home-built trigger circuit. A ring-down event was initiated when the detector signal reached a preset threshold value, triggering the switch-off of an inline acousto optic modulator (Housego Fibre-Q, Gooch) located between the laser and the fiber collimation package. The detector signal was simultaneously fed to a USB data acquisition unit (NIUSB6356, National Instruments), which was controlled by a custom LabVIEW (National Instruments) program running on a standard PC used for further averaging and processing of the data. The laser was tuned by changing the temperature and keeping the current constant, whereby the wavelength was calibrated with a wave meter.

In order to avoid dust particles crossing the laser beam, the cavity was enclosed by an aluminium box with an acrylic glass lid and quartz windows (volume: 36.8 l), which had openings on the sides to enable gas exchange with the laboratory air. On top of the lid, the plasma jet was fixed on a micrometer stage to allow movements in all directions relative to the intra-cavity laser beam. From previous investigations it is known, that the effluent has a cylindrical shape [30]. Figure 2 shows a schematic of the coordinate system used.

Side
view

Top
view

kINPen

$z = 0$

y

$z = 0$

x

$(0, 0, z)$

Laser beam

y

nozzle

l

x

$(0, 0)$

Laser beam
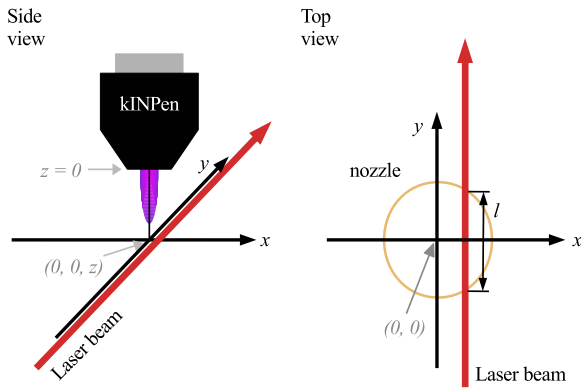
Figure 2. Schematic of the coordinate system with the definitions of x, y, z and the effective absorption length l.
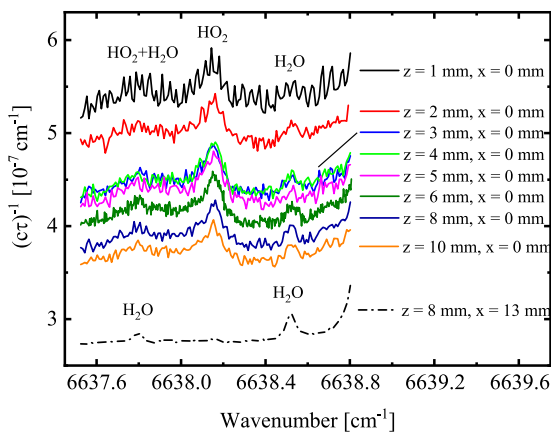
Figure 3. The cavity losses $\frac{1}{c\tau}$ as a function of wavenumber for different z-distances (1 to 10 mm at $x = 0$ mm and $z = 8$ mm at $x = 13$ mm).

In the following, z is defined as the distance from the nozzle outlet to the laser beam along the symmetry axis of the effluent of the plasma jet. The y-axis is defined as the axis parallel to the propagation direction of the intracavity laser beam, which crosses the effluent of the plasma jet in its centre, and the x-axis is perpendicular to that. The effective absorption length l is given by the intersection at given positions x and z of the absorption cylinder (see figure 2).

In order to obtain a spatial map for the HO_2 distribution in the effluent of the plasma jet, the absorption coefficient of HO_2 at various x and z positions is required. This was achieved by acquiring ring-down data at discrete wavelengths as the laser was tuned from 6637.6 to 6638.7 cm^{-1}.

In figure 3, the cavity loss spectra $\frac{1}{c\tau(\nu)}$ through the centre of the effluent ($x = 0$ mm) at various axial positions between $z = 1$ mm and $z = 10$ mm are depicted together with a spectrum taken at $z = 8$ mm and $x = 13$ mm, where $\tau(\nu)$ is the measured ring-down time at frequency ν and c is the speed of light in vacuum. Each spectral point shows the average loss rate calculated from 200 ring-down events. We identified the strongest HO_2 absorption at 6638.21 cm^{-1} and two absorption features of water at 6638.57 cm^{-1} and 6637.85 cm^{-1}. Beyond the effluent at $x = 13$ mm, absorption from water

transitions was dominant and the absorption by HO_2 barely visible. Between 6638.33 cm^{-1} and 6638.49 cm^{-1}, the absorption by water and HO_2 is small compared to other cavity losses. We used the mean and the standard deviation of that region in order to compare the plasma-induced cavity losses without absorption features and the noise in the spectra at the different z-positions.

At $x = 13$ mm and $z = 8$ mm, the cavity losses without absorption were lower by a factor of 1.4 compared to the spectrum through the centre of the effluent at the same axial position. Additionally, the noise on the spectra decreased by a factor of 2.2 for $x = 13$ mm and $z = 8$ mm compared to $x = 0$ mm and $z = 8$ mm. Measuring through the centre of the effluent, the cavity losses without absorption increased from $3.6 \cdot 10^{-7}$ cm^{-1}, when the jet was located at $z = 10$ mm, to $5.4 \cdot 10^{-7}$ cm^{-1} for $z = 1$ mm, whereas the noise on each spectrum increased proportional to $z^{-0.5}$. This demonstrates, how the plasma interferes with the cavity modes introducing additional fluctuations on the cavity losses due to fast changes in the refractive index and gas turbulences.

For the determination of the HO_2 density, a correct evaluation of the base line is crucial, which corresponds to a determination of the cavity losses induced by the plasma without absorbing species. This is possible by applying a fitting procedure of a full spectrum that simulates the absorption features in order to separate absorption and non-absorption losses.

2.3. Derivation of total number densities of HO_2 from cavity ring-down spectra

The procedure to obtain total number densities from CRDS spectra is described in detail in reference [18]. With CRDS, the total cavity loss rate as a function of frequency ν is measured, which is inversely proportional to the ring-down time and includes all possible loss mechanisms, such as light transmission through the cavity mirrors, absorption within the dielectric coating of the mirrors, diffraction losses, scattering by the sample (e.g., due to changes in the refractive index and gas turbulences), and optical absorption, in particular, of the molecules to be detected. Over the typical range of a measured spectrum, only the optical absorption is strongly frequency dependent, so the other loss mechanisms can be described by a straight line defined by the constant b_0 and a non-zero gradient $b_1\nu$ accounting for slow changes of the mirror reflectivity and thus of the ring-down time, due for example to material deposition on the high reflectivity mirror coatings.

In addition to the HO_2 concentration located over a distance l, the contribution of water that is assumed to be homogeneously distributed over the whole cavity length L needs to be considered. The frequency-dependent absorption coefficient $\alpha(\nu)$ is then given by

$$\alpha(\nu) = \frac{1}{c}\left[\frac{1}{\tau(\nu)} - \frac{1}{\tau_0(\nu)}\right] \tag{1}$$

$$= \frac{1}{c}\frac{1}{\tau(\nu)} - [b_0 + b_1\nu] \tag{2}$$

$$= [H_2O]\,\sigma_W(\nu) + \frac{l}{L}[HO_2]\,\sigma_H(\nu) + \epsilon(\nu), \tag{3}$$

Table 1. Line positions, line strengths and assignment (as known so far [33]) for the considered HO_2 transitions, measured by Thiebaud *et al* [32] and determined by Gianella *et al* [18].

Transition frequency cm^{-1}	Line strength $\times 10^{-21}$ cm^2 cm^{-1}	Assignment [33]
6637.47	1.00	$^qP_0(13)$
6637.60	0.99	$^qP_0(13)$
6637.64	1.11	
6637.74	1.67	
6637.78	1.28	$^qQ_3(4)$
6637.83	1.16	$^qQ_3(5)$
6637.85	1.66	
6637.87	1.12	$^qQ_3(6)$
6637.89	0.89	$^qQ_3(7)$
6637.95	0.79	
6637.97	0.87	$^qQ_3(8)$
6638.00	1.04	$^qQ_3(9)$
6638.04	1.04	
6638.12	3.86	$^qP_0(6)$
6638.16	0.67	
6638.21	7.09	$^qQ_3(4\text{--}9)$
6638.40	0.65	
6638.44	0.49	
6638.52	0.32	
6638.59	0.92	
6638.70	0.46	
6638.74	3.06	$^qP_1(5)$
6638.76	1.37	$^qP_1(5)$

where c is the speed of light, $\tau(\nu)$ is the measured ring-down time, τ_0 is the ring-down time of a cavity without absorbing species, $[H_2O]$ and $[HO_2]$ are the molecular densities of water (W) and HO_2 (H); $\sigma_W(\nu)$ and $\sigma_H(\nu)$ are the frequency-dependent absorption cross-sections for water and HO_2, respectively, and $\epsilon(\nu)$ is the residual.

One difficulty when determining the absolute species density is the necessity to use an (often unknown) absorption cross-section. Furthermore, the absorption lines are significantly broadened by pressure broadening at atmospheric pressure and have to be described by an area normalized Voigt profile $\mathscr{V}\left(\nu - \nu_0^{(t)}; \gamma\right)$. However, the pressure broadening coefficient γ for the transition t with the frequency ν_0 is also often unknown. For overlapping transitions, the total absorption cross-section $\sigma(\nu; \gamma)$ is composed of the superposition of the contributions for all transitions t at frequency ν

$$\sigma(\nu; \gamma) = \sum_t \mathscr{S}^{(t)} \mathscr{V}\left(\nu - \nu_0^{(t)}; \gamma\right), \qquad (4)$$

where $\mathscr{S}^{(t)}$ is the line strength of transition t.

Here, the absorption cross-sections for transitions of the combination bands $2\nu_2 + \nu_3$ and $3\nu_2 + \nu_3$ of water were taken from Gianella *et al*; they have computed σ_W for different mixtures of Ar:O_2:N_2 using the tabulated line strengths in the HITRAN database [31] and experimentally determined pressure broadening coefficients [18].

For HO_2, spectroscopic data are relatively rare, as these radicals are difficult to produce with a known quantity. Thiebaud *et al* reported transitions of HO_2 between 6638.7 cm^{-1} and
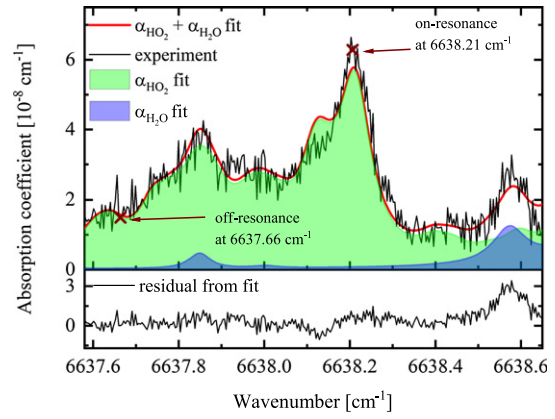
Figure 4. Baseline corrected absorption coefficient spectrum for 3 slm Ar with 3000 ppm water in the feed gas and a 5 slm oxygen gas curtain, taken at $x = 0$ mm and $z = 6$ mm (black line) together with the corresponding fit (red line, see equation (3)) with the individual contributions of water (blue surface) and HO_2 (green surface). Also given is the residual of the fit.

6637.6 cm^{-1} measured in 50 Torr of helium [32] and Gianella *et al* have visually determined all the significant transitions in that range [18]. Table 1 shows the considered line positions with the corresponding line strengths and assignments [33]. Only Ibrahim *et al* reported air-broadening coefficients for 34 HO_2 transitions between 6631 cm^{-1} and 6671 cm^{-1} with values ranging from 0.078 to 0.154 cm^{-1} atm^{-1} (half width at half maximum) [34]. For our argon-water-oxygen mixture, significantly different values should be expected. Gianella *et al* determined the pressure broadening of HO_2 in argon-water-oxygen-nitrogen mixtures to be between 0.040 and 0.072 cm^{-1} atm^{-1} depending on the composition of the curtain gas, using a fitting routine of full spectra based on equations (3) and (4), where γ_H was assumed to be constant for all considered transitions [18, 28].

Using the same fitting routine as described in reference [18] for our absorption spectra, we determined the pressure broadening coefficient γ_H, the baseline coefficients b_0, b_1, and the densities $[H_2O]$ and $[HO_2]$. An example spectrum, taken at $x = 0$ mm and $z = 6$ mm, is shown in figure 4, together with the fit for the contributions of water and HO_2 and the corresponding residual from the fit. In this case, γ_H was determined to be 0.043 ± 0.004 cm^{-1} atm^{-1}. The pressure broadening coefficient has about the same value for all measured z-positions and is close to the value Gianella *et al* have reported [18, 28]. From gas flow experiments and simulations it is known that the gas flow through the plasma jet is turbulent [35, 36], resulting in an effective mixing of feed and curtain gases. Under these conditions, the assumption to use the same pressure broadening coefficient for all axial and radial positions seems to be valid. However, to obtain a full spectrum at a specific radial and axial position, a few hundred data points need to be recorded, whereby each data point was determined by averaging 200 single ring-down events. This procedure takes about 1 h, and achieving a map of the spatial density distribution of HO_2 becomes time consuming. In order to reduce the acquisition time significantly, we applied the on/off-resonance method discussed in the next section.

3. Results

3.1. On/off-resonance method to obtain absorption coefficients

The on/off-resonance method is based on the measurement of the cavity losses at only two different wavelength positions. For the first position, we chose $\nu_{on} = 6638.21$ cm^{-1}, where the absorption of HO$_2$ has the highest absorption cross-section, hence called on-resonance (see figure 4). At this position, the absorption cross-section of water is several orders of magnitude lower than the cross-section of HO$_2$, so that the contribution of water can be neglected even at densities of water in the range of 10^{17} cm^{-3} expected for ambient conditions. Unfortunately, there was no wavelength position without a contribution of HO$_2$ within the tuning range of the laser. Therefore, we selected $\nu_{off} = 6637.66$ cm^{-1} for the off-resonance position, because of the negligible contribution of water and the lower density of HO$_2$ (see figure 4). Since the gradient of the base line was assumed to be small, the residual for both wavelength positions is similar. Taking the difference of the cavity losses at the two chosen wavenumbers and using equation (3), we determined the difference in the absorption coefficient $\Delta\alpha$ to be

$$\Delta\alpha = \frac{1}{c\tau(\nu_{on})} - \frac{1}{c\tau(\nu_{off})} \quad (5)$$

$$= [HO_2]\frac{l}{L}(\sigma_H(\nu_{on}) - \sigma_H(\nu_{off})) \quad (6)$$

$$= [HO_2]\frac{l}{L}\Delta\sigma_H. \quad (7)$$

We obtained $\Delta\sigma_H = (4.5 \pm 0.4) \cdot 10^{-20}$ cm^2 from a fit of the full absorption spectrum (see figure 4) with a pressure broadening coefficient of 0.043 ± 0.004 cm^{-1} atm^{-1} that was assumed to be the same for all axial and radial positions.

For each on- and off-resonance wavelength position, 2800 ring-down events were recorded and the mean value and the standard deviation were calculated to determine $\Delta\alpha$, where the error in $\Delta\alpha$ corresponds to $\delta\alpha = \sqrt{\delta_{on}^2 + \delta_{off}^2}$ with the standard deviations δ_{on} and δ_{off} for on- and off-resonance position, respectively.

In figure 5, values for $\Delta\alpha$ at $x = 0$ mm derived from the on/off-resonance measurements as a function of z are shown together with values of $\Delta\alpha$ obtained from a fit of full spectra for various z-positions. Within the error, both data sets agree with each other. As the on/off-resonance method gives similar results to the recording of full spectra, we concluded, that it is sufficient to measure at two wavelength positions, on- and off-resonance, in order to obtain the densities of HO$_2$.

To calculate absolute number densities, the effective absorption path length l, over which HO$_2$ is distributed, has to be known at each z-position. This point is discussed in the next section.

3.2. Determination of the effective absorption length of HO$_2$

In order to determine the effective absorption length as a function of z, we measured the difference in the absorption coefficient $\Delta\alpha$ at various x-positions in steps of $\Delta x = 0.25$ mm
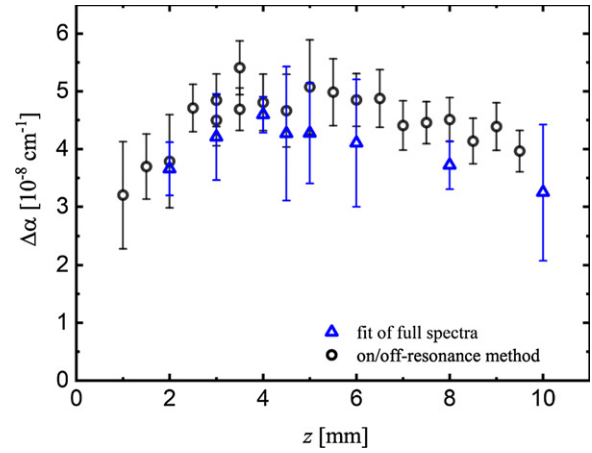
Figure 5. $\Delta\alpha$ as a function of z at $x = 0$ mm, obtained from on-off-resonance measurements and from a fit of full spectra.

over the complete diameter of the effluent. In figures 6(a)–(e) the measured values for $\Delta\alpha$ as a function of the distance to the symmetry axis through the effluent centre x at $z = 2, 4, 6, 8,$ and 10 mm, respectively, are presented. All radial scans could be described by a Gaussian function, whose width increased with increasing z-distance according to

$$\Delta\alpha(x, z) = \frac{A(z)}{w(z)\sqrt{\frac{\pi}{2}}} \exp\left\{-2\left(\frac{x - x_c}{w(z)}\right)^2\right\} + \Delta\alpha_{off}, \quad (8)$$

where $A(z)$ is the area of the Gaussian function obtained at the position z, $w(z)$ is the Gaussian width at the position z, x_c is the centre position of the Gaussian function at the position z, and $\Delta\alpha_{off}$ is an offset-value. We determined w to be 1.73 ± 0.20 mm at $z = 2$ mm and 1.51 ± 0.08 mm at $z = 4$ mm, respectively, which is consistent with the diameter of the plasma jet nozzle, which is 1.6 mm. Between $z = 4$ mm and $z = 10$ mm, w increased linearly with

$$w(z \geqslant 4 \text{ mm}) = (0.17 \pm 0.02) \cdot (z - 4) + (1.52 \pm 0.16) \text{ mm}. \quad (9)$$

In order to determine the HO$_2$ concentration in the effluent, the effective absorption length l was defined by

$$l(z) = 2.576 \cdot w(z), \quad (10)$$

the distance between the base points of the Gaussian distributions, which represent the limits containing 99% of the area of the Gaussian functions. We obtained an effective absorption length l, which was constant at $l = (3.9 \pm 0.5)$ mm between $z = 2$ mm to $z = 4$ mm and increased linearly to $l = (6.7 \pm 0.1)$ mm from $z = 4$ mm to $z = 10$ mm. From schlieren measurements, gas flow observations and simulations it is known that within the first 4 mm below the nozzle, the effluent diameter remains constant, which is in agreement with our observations, taking the error into account. Furthermore, the values for l as a function of z are in agreement (within 10%) with those investigations [30, 35].

In figure 7, the densities of HO$_2$ are displayed as a function of z, obtained from the on/off-resonance measurement at $x = 0$ mm and from fits of full spectra at $x = 0$ mm. The

(a) $z = 2$ mm

(b) $z = 4$ mm


(c) $z = 6$ mm

(d) $z = 8$ mm

(e) $z = 10$ mm
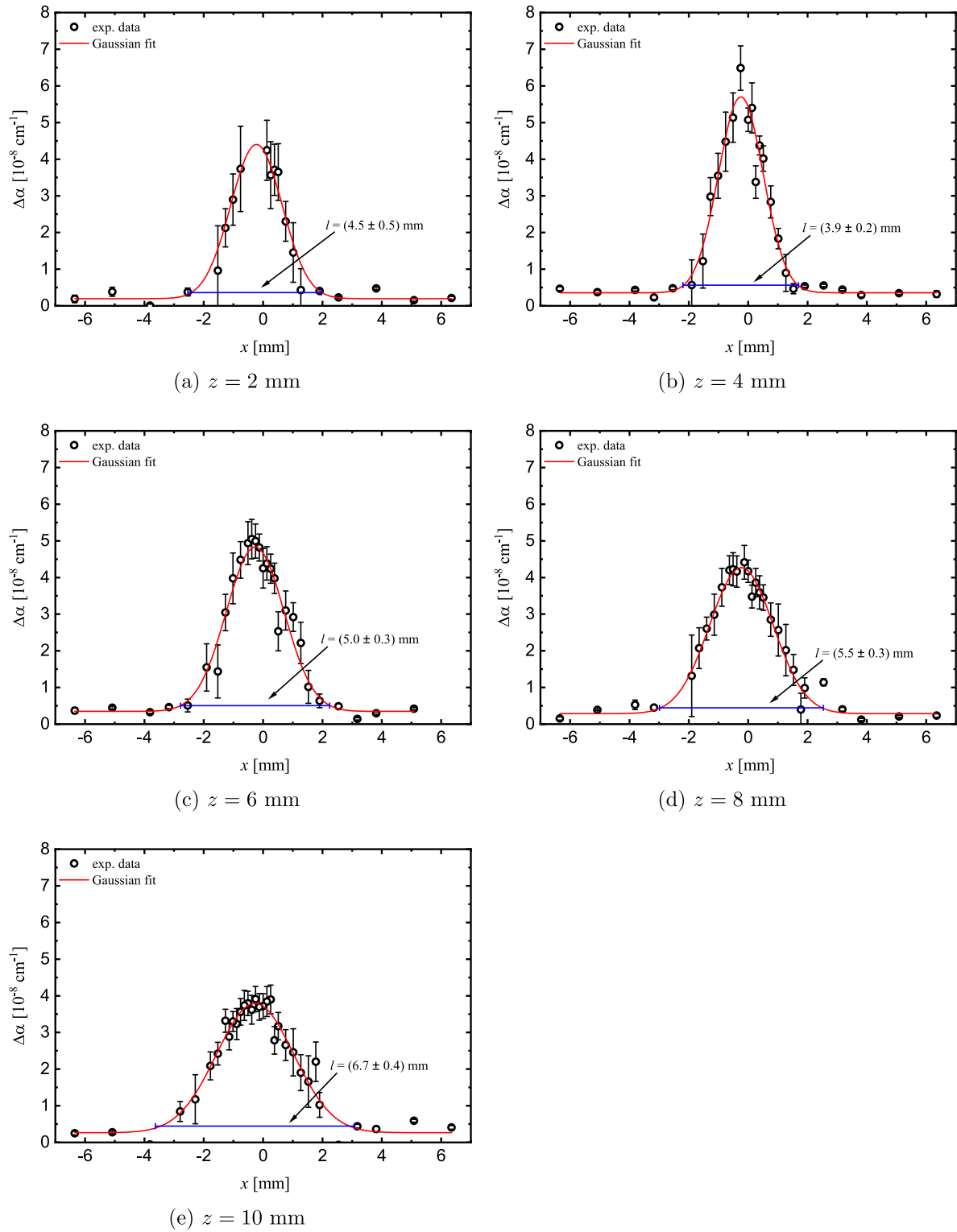
Figure 6. $\Delta\alpha$ as a function x at various z-positions together with Gaussian fits.

absolute number densities were determined by using an effective absorption length l as given in equation (10). Therefore, a homogeneous distribution of HO_2 over the diameter l was assumed. Within the error, the densities obtained from both methods are in agreement with each other. Between $z = 1$ mm and $z = 4$ mm the density of HO_2 increased from $(1.4 \pm 0.4) \cdot 10^{14}$ cm^{-3} to a maximum of about $(2.3 \pm 0.3) \cdot 10^{14}$ cm^{-3}.

After this, the density of HO_2 decreased linearly with increasing z to $(0.85 \pm 0.12) \cdot 10^{14}$ cm^{-3} at $z = 10$ mm. The density at $z = 10$ mm is about 2 times higher than the density obtained by Gianella *et al* corrected for the difference in the enhanced absorption length [18]. This could be due to a higher resolution positioning system used in the current work, and the fact that the current kINPen device is of a different age than that
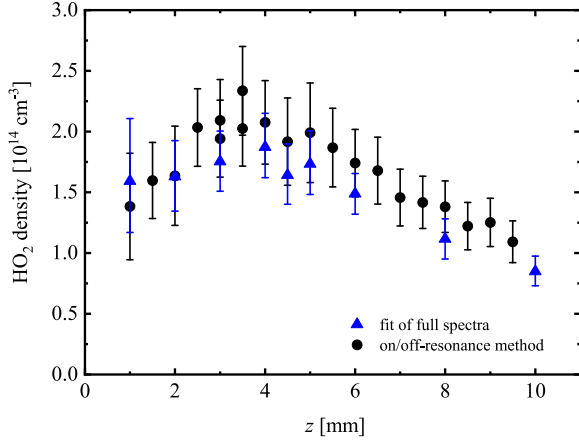
Figure 7. Line-of-sight averaged density of HO_2 as a function of z at $x = 0$ mm obtained by on/off-resonance measurements and by a fit of full spectra. The number densities were evaluated for $l(z) = 2.576 \cdot w(z)$, where $w(z)$ is the width of the radial distributions at each z-position.

used previously [18, 28]. It should be emphasised, however, that the difference in number density is only a factor of two, and the trends and the deduced reaction chemistry show good consistency within the operating parameters.

For all Gaussian fits, we determined a small offset value $\Delta\alpha_{off}$, indicating an absorption of HO_2 which is distributed beyond the effluent diameter. Using this offset value for equation (7) and assuming an absorption length $l = L = 80$ cm, we obtained a mean background density of $n_b = (6.5 \pm 1.5) \cdot 10^{10}$ cm^{-3} for all radial scans. This background density is also about a factor of 2 higher than that obtained previously in reference [18].

How the spatial distribution of HO_2 in three dimensions can be obtained by using the on/off-resonance method is discussed in the next section.

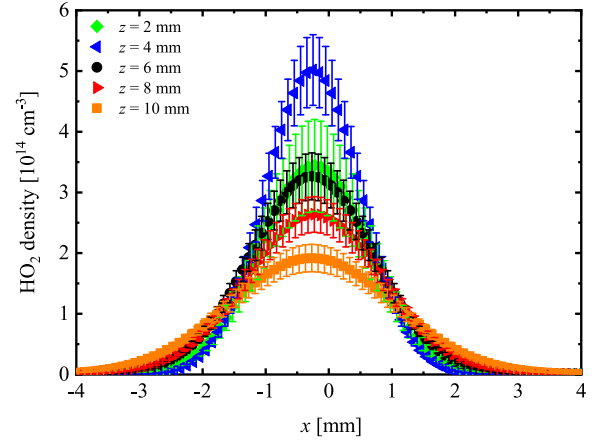### 3.3. Determination of the spatial distribution of HO_2

To determine a radial density distribution for an axially symmetric sample from a line-of-sight measurement as given by CRDS, the line-of-sight absorption is measured at different radial positions x maintaining the z-position and scanning at least half of the sample's diameter.

With the on/off-resonance method, we determined that the radial scans are Gaussian-like with a Gaussian distribution in $\Delta\alpha$ (see equation (8)). Performing an Abel inversion, $\mathscr{A}$, on such a radial scan and with a coordinate transformation $x \rightarrow \tilde{x} = x - x_c$, we obtain the absorption coefficient $\Delta\alpha(\rho, z)$, which is constant on a circle with a given radius $\rho = \sqrt{(x - x_c)^2 + y^2}$ with the centre position $(x_c, 0)$ and at the axial position z:
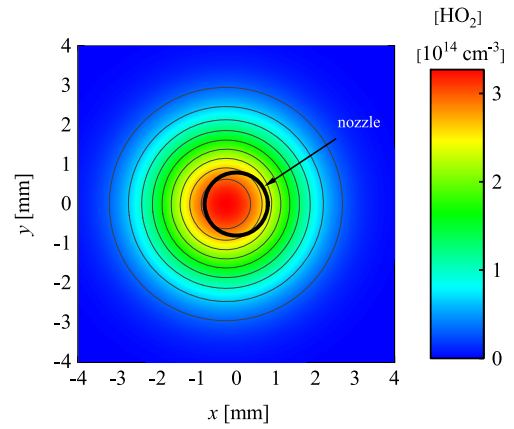
$$\Delta\alpha(\rho, z) = \mathscr{A}\left[\Delta\alpha(x, z)\right] \quad (11)$$

$$= -\frac{1}{\pi} \int_{\rho}^{\infty} \frac{\mathrm{d}\Delta\alpha(\tilde{x}, z)}{\mathrm{d}\tilde{x}} \frac{\mathrm{d}\tilde{x}}{\sqrt{(x - x_c)^2 - \rho^2}} \quad (12)$$

$$= \frac{2}{\pi} \frac{A(z)}{w^2(z)} \exp\left\{-2\frac{\rho^2}{w^2(z)}\right\} \quad (13)$$

Figure 8. Density of HO_2 as a function of x for $y = 0$ and $z = 2, 4, 6, 8,$ and 10 mm.

Figure 9. Density distribution of HO_2 as a function of x and y at $z = 6$ mm together with a shape of the nozzle outlet. The maximum of the distribution is slightly shifted with respect to the centre of the effluent.

Considering the uncertainties $\delta A(z)$ and $\delta w(z)$ of the area and the width, respectively, obtained from the fitting procedure of the experimental radial scans by a Gaussian function, the uncertainty of $\Delta\alpha(\rho, z)$ can be expressed by
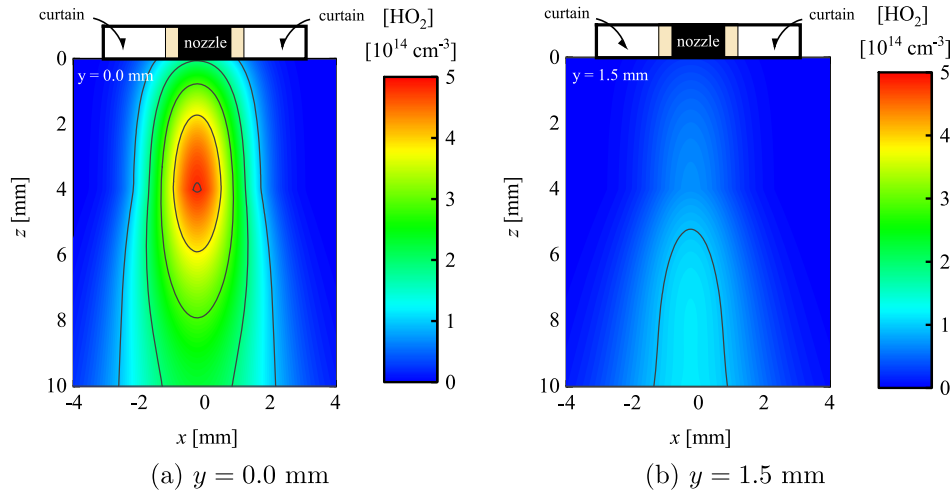
$$\delta\Delta\alpha(\rho, z)$$
$$= \sqrt{\left(\frac{\Delta\alpha(\rho, z)\delta A(z)}{A(z)}\right)^2 + \left(\frac{4A(z)\exp\left\{-2\rho^2/w^2(z)\right\}\delta w(z)}{\pi w^5(z)}\right)^2}.$$
$$(14)$$

The spatial density of HO_2 can then be calculated by using equation (7)

$$[HO_2](x, y, z) = \frac{\Delta\alpha(\rho, z)}{\Delta\sigma_H}L, \quad (15)$$

and the error is given by

$$\delta[HO_2](x, y, z) = \sqrt{\left(\frac{\delta\Delta\alpha(\rho, z)}{\Delta\sigma_H}L\right)^2 + \left(\frac{\Delta\alpha(\rho, z)\delta\Delta\sigma_H}{(\Delta\sigma_H)^2}L\right)^2},$$
$$(16)$$

Figure 10. Localised density of HO$_2$ illustrated in two different planes cut along the symmetry axis of the plasma jet at two y-positions.

with $\delta\Delta\sigma_H = 0.4 \cdot 10^{-20}$ cm^2.

In figure 8, the density distributions of HO$_2$ as a function of x for $y = 0$ mm and for various z-positions are depicted. An inter-sectional area of the distribution of HO$_2$ as a function of x and y at $z = 6$ mm is illustrated in figure 9 together with a shape of the nozzle outlet, which was shifted by $x_c = 0.23$ mm compared to the maximum of the HO$_2$ density.

Since all radial profiles have a Gaussian shape with increasing width for an increasing z-distance, we can determine the spatial distribution of HO$_2$ along the symmetry axis of the effluent by a combination of an axial scan of the absorption coefficient $\Delta\alpha(x = 0, z)$, which is given in figure 5 and by equation (8), and by using equation (13) and equation (15) to

$$[\text{HO}_2](x,y,z) = \frac{L}{w(z)\sqrt{\frac{\pi}{2}}} \frac{\Delta\alpha(x=0,z) \ \exp\left\{-2\frac{\rho^2 - x_c^2}{w^2(z)}\right\}}{\Delta\sigma_H}. \tag{17}$$

In order to obtain the localised density of HO$_2$ along the symmetry axis of the plasma jet as a function of x and z at various y positions, we interpolated between the measured values for the effective absorption length to achieve a function for $w(z)$. Furthermore, we used a third order polynomial fit to describe the absorption coefficient $\Delta\alpha(x = 0, z)$ as a function of z (see figure 5). In figure 10(a) and (b), the localised densities of HO$_2$ along the axis of symmetry at $y = 1.5$ mm, and $y = 0$ mm are demonstrated. These figures show that it is possible to obtain the spatial distribution of HO$_2$ in the effluent (in three dimensions) of the kINPen with cw-CRDS by measuring the absorption along the symmetry axis and the radial distribution at different z-positions.

4. Discussion

Previously, Gianella *et al* investigated the radial distribution of HO$_2$ produced in a CAPJ by sampling the effluent over a pinhole and expanding it to 5.33 kPa. At low pressure, they obtained a doughnut-like shape with the maximum HO$_2$ density at $\rho = 1$ mm and a dip in the centre. According to their

findings, they proposed a production of HO$_2$ by the reaction of H atoms, formed by the dissociation of water in the plasma zone and the effluent, and oxygen, which diffused from the surrounding atmosphere into the effluent. They also mentioned that the experimental procedure could be the reason for the observed profile and that further investigations were necessary [18].

Here, we determined the spatial distribution at atmospheric pressure in the effluent directly and observed a Gaussian distribution in radial direction that has its maximum at the centre of the effluent (see figure 8). This centre was slightly shifted with respect to the symmetry axis through the centre of the nozzle (see figure 9), which could be explained by an asymmetry in the filamentary discharge in the plasma zone of the plasma jet, where one direction for the filament is preferred. In this direction, the production of H atoms is larger than in the overall plasma zone leading to a formation of HO$_2$, which has its maximum off the centre.

The spatial distribution of HO$_2$ in the effluent at $y = 0$ mm, as depicted in figure 10(a), shows first an increase of the density of HO$_2$ on the symmetry axis starting from $(1.8 \pm 0.6) \cdot 10^{14}$ cm^{-3} at the nozzle outlet to its maximum concentration of $(4.8 \pm 0.6) \cdot 10^{14}$ cm^{-3} at about 4 mm below the nozzle. After that, the density gradually decreases to $(2.0 \pm 0.6) \cdot 10^{14}$ cm^{-3}.

The density of HO$_2$ at $z = 0$ mm would imply an effective diffusion of the gas curtain into the effluent beginning at the nozzle outlet, which is in contrast to the investigations by Dünnbier *et al* [37] and by Schmidt-Bleker *et al* [38]. Both determined that the effective diffusion of oxygen from the gas curtain starts at about 4 mm below the nozzle. Hence, we concluded that part of the HO$_2$ was already produced in the plasma zone inside the kINPen device. Therefore, a certain amount of oxygen has to be present within the feed gas.

Winter *et al* investigated the feed gas humidity in the plasma jet for different kinds of gas tubing, metal and polymeric tubing [13]. The initial water concentration in polymeric tubing was about 1000 ppm, which could be reduced to less than 70 ppm after 3 h purging. This initial water concentration can

be explained by diffusion of water vapour from ambient air into the tubing. As the kINPen-Sci, investigated in this work, was built with the same polymeric tubing a feed gas humidity of about 100 ppm after 15 min argon flow can be expected. If water from the surrounding atmosphere can diffuse into the tubing, it is not unreasonable to assume that O_2 and N_2 can diffuse into the gas tubing and thus into the feed gas as well. Based on the permeability of the tubing for oxygen and nitrogen, we conclude that the amount of diffused oxygen through the gas tubing is insufficient on its own to explain the HO_2 densities measured close to the nozzle.

An additional source of oxygen in the plasma zone can be found by considering the discharge dynamics of the kINPen. From previous investigations of the kINPen it is known that the discharge behaviour is similar to the guided streamer formation that occurs in kHz plasma jets [21, 39]. Schmidt-Bleker *et al* observed a backwards directed excitation wave (opposite to the gas flow) in a kINPen operated in helium, which required the presence of oxygen in the curtain gas. The speed of this backwards directed excitation wave was 4200 m s^{-1} for a pure O_2 curtain [38], which is much higher than the gas flow of about 25 m s^{-1}. Reuter *et al* also observed a similar feature when operating the kINPen in argon [40]. With this backwards directed excitation wave, air can diffuse into the plasma zone resulting in a source of oxygen [41], which would lead to a significant formation of HO_2 at the nozzle outlet. This aspect of the discharge dynamics and its influence on the reaction kinetics deserves further attention.

Finally, in figure 10(b), the spatial distribution of HO_2 along the symmetry axis at $y = 1.5$ mm is shown. A significant HO_2 density could only be determined starting from $z = 4$ mm. This could either be due to the size of the effluent that starts widening at $z = 4$ mm or can be caused by a production of HO_2 by oxygen from the surrounding atmosphere. In the latter case, a significant density of H atoms needs to be present 4 mm below the nozzle at $y = 1.5$ mm. Therefore, further investigations are required.

It is clear that a simple plug flow model cannot fully explain the spatial distribution of HO_2. Furthermore, the determined spatial distribution of HO_2 clearly demonstrates that for a reaction kinetics model, the plasma zone needs to be considered as well as the outward diffusion of the effluent gas and the inward diffusion of the surrounding atmosphere.

5. Conclusion

This work has successfully demonstrated that CRDS can deliver spatial information about the density distribution of transient species. Furthermore, it is shown that instead of taking full spectra the on/off-resonance method is a viable technique to determine absolute number densities by measuring the absorption at two wavelengths, which reduces the acquisition time significantly.

We employed a cavity ring-down spectrometer with a cw-laser source emitting at 1506.4 nm (6638.2 cm^{-1}) in order to investigate the spatial distribution of HO_2 in the effluent of the cold atmospheric pressure plasma jet kINPen-Sci. By sampling the effluent perpendicular to the laser beam along

the *x*-axis, we determined the distance *l*, over which HO_2 was distributed. All measured distributions have a Gaussian shape. We obtained an effective absorption length *l*, which was constant at $l = (3.9 \pm 0.5)$ mm between $z = 2$ mm to $z = 4$ mm and increased linearly to $l = (6.7 \pm 0.1)$ mm from $z = 4$ mm to $z = 10$ mm. Accordingly, we calculated the line-of-sight averaged density distribution of HO_2 along the symmetry axis.

In order to determine the spatial distribution of HO_2, we performed an Abel inversion on the Gaussian distributions of the radial scans. By a combination of the radial distributions and an axial scan of the absorption coefficient along the *z*-axis, we obtained the localised density of HO_2 along the symmetry axis of the effluent in *x* and *z* direction. The maximum HO_2 concentration of $(4.8 \pm 0.6) \cdot 10^{14}$ cm^{-3} was found on the symmetry axis through the centre of the nozzle at $z = 4$ mm, which corresponds to a line-of-sight averaged density of $(2.3 \pm 0.3) \cdot 10^{14}$ cm^{-3}.

From the local HO_2 density of $(1.8 \pm 0.6) \cdot 10^{14}$ cm^{-3} at the outlet of the nozzle, we concluded that a significant density of HO_2 was produced within the plasma zone of the plasma jet. This requires a source of oxygen in the plasma zone, which is most likely due to diffusion of ambient air into the capillary caused by a backwards directed excitation wave and by diffusion into the gas tubing.

For a more detailed analysis of the reaction cycle of HO_2, the spatial distribution of H atoms in the effluent and a 2-dimensional reaction kinetics model that includes reactions in the plasma zone and the effluent, considering also the radial diffusion of the surrounding atmosphere, are required and are part of further investigations.

ORCID iDs

S-J Klose ⓘ https://orcid.org/0000-0003-4517-0268
K M Manfred ⓘ https://orcid.org/0000-0002-6850-1560
G A D Ritchie ⓘ https://orcid.org/0000-0003-1663-7770
J H van Helden ⓘ https://orcid.org/0000-0001-8925-2607

References

[1] Laroussi M and Akan T 2007 *Plasma Process. Polym.* **4** 777–88
[2] Penkov O V, Khadem M, Lim W S and Kim D E 2015 *J. Coat. Technol. Res.* **12** 225–35
[3] Fanelli F and Fracassi F 2017 *Surf. Coat. Technol.* **322** 174–201
[4] von Woedtke T, Reuter S, Masur K and Weltmann K D 2013 *Phys. Rep.* **530** 291320
[5] Ito M, Oh J S, Ohta T, Shiratani M and Hori M 2017 *Plasma Process. Polym.* **15** e201700073

[6] Winter J, Brandenburg R and Weltmann K D 2015 *Plasma Sources Sci. Technol.* **24** 064001

[7] Weltmann K D and von Woedkte T 2017 *Plasma Phys. Control. Fusion* **59** 014031

[8] Fridman A and Friedman G (ed) 2013 *Plasma Medicine* (Chichester: John Wiley and Sons Ltd)

[9] Privat-Maldonado A, Schmidt A, Lin A, Weltmann K D, Wende K, Bogaerts A and Bekeschus S 2019 *Oxid. Med. Cell. Longevity* **2019** 9062098

[10] Keidar M 2015 *Plasma Sources Sci. Technol.* **24** 033001

[11] Reuter S, Tresp H, Wende K, Hammer M U, Winter J, Masur K, Schmidt-Bleker A and Weltmann K D 2012 *IEEE Trans. Plasma Sci.* **40** 2986–93

[12] Reuter S, Winter J, Iséni S, Schmidt-Bleker A, Dünnbier M, Masur K, Wende K and Weltmann K D 2015 *IEEE Trans. Plasma Sci.* **43** 3185–92

[13] Winter J, Wende K, Masur K, Iseni S, Dünnbier M, Hammer M U, Tresp H, Weltmann K D and Reuter S 2013 *J. Phys. D: Appl. Phys.* **46** 295401

[14] Gaens W V, Iseni S, Schmidt-Bleker A, Weltmann K D, Reuter S and Bogaerts A 2015 *New J. Phys.* **17** 033003

[15] Jablonowski H and von Woedtke T 2015 *Clinical Plasma Med.* **3** 42–52

[16] Wende K, von Woedtke T, Weltmann K D and Bekeschus S 2018 *Biol. Chem.* **400** 1437–4315

[17] Kapaldo J, Han X and Ptasinska S 2019 *Plasma Process. Polym.* **16** e1800169

[18] Gianella M, Reuter S, Press S A, Schmidt-Bleker A, van Helden J P H and Ritchie G A D 2018 *Plasma Sources Sci. Technol.* **27** 095013

[19] Panov A 2018 *Mol. Biol.* **52** 295–305

[20] Ikawa S, Kitano K and Hamaguchi S 2010 *Plasma Process. Polym.* **7** 33–42

[21] Reuter S, Sousa J S, Stancu G D and van Helden J P H 2015 *Plasma Sources Sci. Technol.* **24** 054001

[22] Peverall R and Ritchie G A D 2019 *Plasma Sources Sci. Technol.* **28** 073002

[23] Gagliardi G and Loock H P (ed) 2014 *Cavity-enhanced Spectrsocopy and Sensing* (Springer Series in Optical Science Vol 179) (Berlin: Springer)

[24] Berden G and Engeln R (ed) 2009 *Cavity Ring-Down Spectroscopy: Techniques and Applications* (Oxford: Wiley-Blackwell)

[25] Lang N, Macherius U, Wiese M, Zimmermann H, Röpcke J and van Helden J P H 2016 *Opt. Express* **24** A537–43

[26] Zaplotnik R, Bišćan M, Krstulović N, Popović D and Milošević S 2015 *Plasma Sources Sci. Technol.* **24** 054004

[27] Benedikt J, Schröder D, Schneider S, Willems G, Pajdarová A and Vlček J 2016 *Plasma Sources Sci. Technol.* **25** 045013

[28] Gianella M, Reuter S, Aguila A L, Ritchie G A D and van Helden J P H 2016 *New J. Phys.* **18** 113027

[29] Reuter S, von Woedtke T and Weltmann K D 2018 *J. Phys. D: Appl. Phys.* **51** 233001

[30] Schmidt-Bleker A, Reuter S and Weltmann K D 2015 *J. Phys. D: Appl. Phys.* **48** 175202

[31] Rothman L *et al* 2013 *J. Quant. Spectrosc. Radiat. Transfer* **130** 4–50

[32] Thiebaud J, Crunaire S and Fittschen C 2007 *J. Phys. Chem.* A **111** 6959–66

[33] DeSain J D, Ho A D and Taatjes C A 2003 *J. Mol. Spectrosc.* **219** 163–9

[34] Ibrahim N, Thiebaud J, Orphala J and Fittschen C 2007 *J. Mol. Spectrosc.* **242** 64–9

[35] Iseni S, Schmidt-Bleker A, Winter J, Weltmann K D and Reuter S 2014 *J. Phys. D: Appl. Phys.* **47** 152001

[36] Semenov I L and Weltmann K D 2020 *Plasma Sources Sci. Technol.* **29** 055001

[37] Dünnbier M, Schmidt-Bleker A, Winter J, Wolfram M, Hippler R, Weltmann K D and Reuter S 2013 *J. Phys. D: Appl. Phys.* **46** 435203

[38] Schmidt-Bleker A, Norberg S A, Winter J, Johnsen E, Reuter S, Weltmann K D and Kushner M J 2015 *Plasma Sources Sci. Technol.* **24** 035022

[39] Bussiahn R, Kindel E, Lange H and Weltmann K D 2010 *J. Phys. D: Appl. Phys.* **43** 165201

[40] Reuter S, Winter J, Iseni S, Peters S, Schmidt-Bleker A, Dünnbier M, Schäfer J, Foest R and Weltmann K D 2012 *Plasma Sources Sci. Technol.* **21** 034015

[41] Gerling T, Brandenburg R, Wilke C and Weltmann K D 2017 *Eur. Phys. J. Appl. Phys.* **78** 10801